Precipitation Associated with Convergence Lines

EVAN WELLER

*School of Earth, Atmosphere and Environment, and Centre of Excellence for Climate System Science,
Monash University, Clayton, Victoria, Australia*

KAY SHELTON

JBA Consulting, Skipton, United Kingdom

MICHAEL J. REEDER AND CHRISTIAN JAKOB

*School of Earth, Atmosphere and Environment, Centre of Excellence for Climate
System Science, Monash University, Clayton, Victoria, Australia*

ABSTRACT

Precipitation is often organized along coherent lines of low-level convergence, which at longer time and space scales form well-known convergence zones over the world's oceans. Here, an automated, objective method is used to identify instantaneous low-level convergence lines in reanalysis data and calculate their frequency for the period 1979–2013. Identified convergence lines are combined with precipitation observations to assess the extent to which precipitation around the globe is associated with convergence lines in the lower troposphere. It is shown that a large percentage of precipitation (between 65% and 90%) over the tropical oceans is associated with such convergence lines, with large regional variations of up to 30% throughout the year, especially in the eastern Pacific and Atlantic Oceans. Over land, the annual-mean proportion of precipitation associated with convergence lines ranges between 30% and 60%, and the lowest proportions (less than 15%) associated with convergence lines occur on the eastern flank of the subtropical highs. Overall, much greater precipitation is associated with long coherent lines (greater than 300 km in length) than with shorter fragmented lines (less than 300 km), and the majority of precipitation associated with shorter lines occurs over land. The proportion of precipitation not associated with any convergence line primarily occurs where both precipitation and frequency of convergence lines are low. The high temporal and spatial resolution of the climatology constructed also enables an examination of the diurnal cycle in the relationship between convergence lines and precipitation. Here an example is provided over the tropical Maritime Continent region.

1. Introduction

Although rainfall is intermittent in both time and space, its timing and location are intimately tied to vertical motion, and the internal circulation of weather systems commonly provides this vertical motion (Birch et al. 2014a; Bony et al. 2015). For this reason, variations in the frequency, structure, or intensity of weather systems exert a strong control on the variability of rainfall. Moreover, the convergence of mass in the low-level boundary layer plays an important role in the initiation and organization of clouds and convection (Reeder and

Smith 1998; Reeder et al. 2013; Birch et al. 2014a, 2015). This initiation and organization is particularly evident over tropical and subtropical latitudes where the majority of precipitation occurs in the vicinity of low-level convergence (Fig. 1).

Low-level convergence is often organized into coherent lines that can be seen in satellite imagery as they are marked by distinct lines of clouds (i.e., Birch et al. 2014a,b). Presumably, these lines are produced by such weather phenomena as the equatorward extension of fronts, gravity waves, atmospheric boundary layer rolls, evaporatively driven cold pools, and topographically generated weather systems such as mountain waves and sea and land breezes. Over longer time scales, persistent sea surface temperature (SST) gradients can also

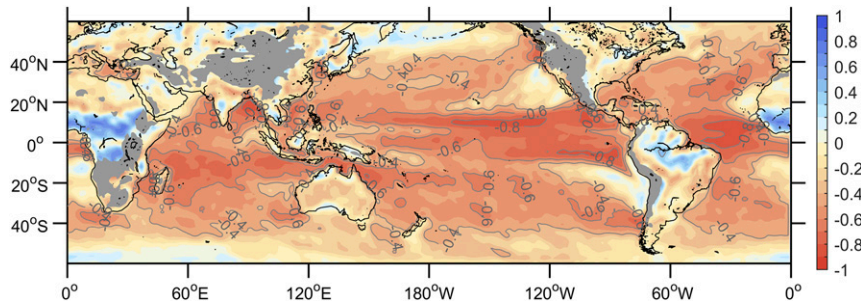*Corresponding author e-mail*: Evan Weller, evan.weller@monash.edu

FIG. 1. Spatial correlation coefficients for 1998–2013 between monthly-mean time series of
CMORPH precipitation rate and 950-hPa layer divergence (calculated using ERA-Interim
winds). Regions where the surface topography is higher than 1 km have been shaded gray.

produce mean vertical circulations and low-level convergence (Lindzen and Nigam 1987). Further, Birch et al. (2014a) examined the role of convergence lines in initiating convection in West Africa and found that although almost all deep convective initiations occurred within patches of local-scale (60 km × 60 km) convergence, half of all initiations occurred in the near vicinity of low-level convergence lines oriented along the mean wind. At longer time and space scales, these individual convergence lines are organized into larger structures such as the intertropical convergence zone (ITCZ) and the South Pacific convergence zone (SPCZ) (Hastenrath 1995; Widlansky et al. 2011; Berry and Reeder 2014; Wodzicki and Rapp 2016).

Predicting rainfall in the tropics remains one of the most important and challenging problems in atmospheric science (IPCC 2007; Flato et al. 2013; Bony et al. 2015). The problem is important because Earth's climate is very strongly affected by deep tropical convection, which drives the wind systems that transport momentum, heat, and water over much of the planet. The problem of predicting rainfall in the tropics is challenging because the main tools for making predictions are numerical models, ranging from those used in numerical weather prediction to those used for climate, which generally handle tropical rainfall poorly and it is not fully understood why (Stephens et al. 2010; Collins et al. 2013). Nonetheless, the way in which convection is represented and the spatial resolution in these models are undoubtedly major factors (Stephens et al. 2010; Stevens and Bony 2013; Birch et al. 2014a; Jakob 2014). On the time scale of a weather forecast, a model's state is predominantly governed by atmospheric processes, but on seasonal and climate time scales, all coupled ocean–land–ice–atmosphere processes become important. Although these models are designed to simulate the main large-scale dynamical processes leading to precipitation (or its suppression), they rely on conceptual parameterizations to represent cloud and microphysical processes. Apart from the rate of emission of the greenhouse gases themselves, the parameterization of convection, especially in the tropics, is generally thought to be one of the biggest sources of uncertainty in climate model projections (Jakob 2014; Rybka and Tost 2014). Many model errors have been ascribed to a poor simulation of convection, which in turn is strongly coupled to the atmospheric circulation. Hence, investigating the relationship between the circulation and the precipitation may provide insights into the performance of models and a better understanding of how atmospheric convection is organized on the scale resolved by the models (Jakob 2010; Catto et al. 2015).

Here, we examine the role of convergence lines (and organized convergence more generally) in organizing precipitation and provide a benchmark by which deficiencies in weather and climate models can be better understood. An automatic objective method is developed to identify convergence lines and the rainfall associated with them. Previous studies have developed methods to automatically identify fronts (Berry et al. 2011a,b) and the associated rainfall (Catto et al. 2012). These studies have shown that large proportions of the rainfall in the major storm-track regions can be associated with fronts. Recent work applying these techniques to climate models has shown much promise in identifying model errors (Catto et al. 2013, 2015). Fronts are just one weather system that initiates and organizes precipitation. Moreover, fronts are themselves but a subset of the larger class of low-level convergence lines in the atmosphere, and are an ineffective feature for examining rainfall in the tropics because fronts and their circulation become weak due to the weak temperature gradients at low latitudes.

The method developed and used in the present study to objectively identify low-level convergence lines is a variation on that described in Berry and Reeder (2014), who used the method to construct a climatology of the ITCZ from reanalyses of mean lower tropospheric

convergence. Wodzicki and Rapp (2016) modified the method outlined by Berry and Reeder (2014) to examine changes in the ITCZ extent and precipitation intensity within the identified ITCZ boundaries in monthly mean data. The benefit of an objective approach is that it avoids any prior human training of the model as in some earlier methods (Bain et al. 2011). However, Berry and Reeder (2014) and Wodzicki and Rapp (2016) adopted long time averaging to isolate continuous line features and isolated tropical features using the lower-troposphere potential temperature.

To associate precipitation with the convergence lines, instantaneous velocity fields are used to identify the lines. From the instantaneous fields of low-level convergence lines, Birch et al. (2014b) developed a climatology of convergence lines over the Arabian Sea and found that it captured the location and offshore propagation of wave-cloud lines from the west coast of India. In the present study, the technique of Berry and Reeder (2014) is applied to a global reanalysis and combined with satellite data to quantify rainfall associated with convergence lines around the globe, including an example examining the diurnal variation of both convergence lines and the associated rainfall over the Maritime Continent. We treat the ERA-Interim global reanalysis as an observed field, but note that the data may include some error in regions with few observations.

Section 2 describes the reanalysis and observational datasets, and the methodology. Section 3 presents annual and seasonal mean global distributions of identified convergence lines and the precipitation associated with them. The results are then discussed and summarized in section 4.

2. Data and methodology

a. Data

The locations of instantaneous convergence lines are computed using the European Centre for Medium-Range Weather Forecasts (ECMWF) interim reanalysis (ERA-Interim; Dee et al. 2011) 6-hourly wind fields at 950 hPa for the period 1979–2013 on a regular 0.75° horizontal grid. This constructed atlas of convergence lines is combined with 6-hourly rainfall on a regular 0.25° horizontal grid from the National Oceanic and Atmospheric Administration (NOAA)/Climate Prediction Center (CPC) morphing technique (CMORPH; Joyce et al. 2004) for the period 1998–2013, when the two datasets overlap in time.

b. Methodology

The current study combines a modified form of Berry and Reeder (2014) used to identify layer- and time-averaged convergence features such as the ITCZ with the approach taken by Catto et al. (2012) to associate precipitation with such objectively identified synoptic features. Modifications are described below and the method is illustrated in Figs. 2 and 3. We conduct our analysis equatorward of 60°, consistent with the spatial extent of the precipitation data.

Instantaneous convergence lines are detected from the locations of the minima in the 6-hourly divergence field calculated at 950 hPa. The wind fields are not averaged in the vertical or time. The method is as follows. First, the points potentially belonging to a convergence line are detected by isolating sufficiently strong regions of convergence. As shown in Fig. 2a, regions in which the divergence is more positive than $-0.1 \times 10^{-5}\,\mathrm{s}^{-1}$ are masked, leaving only regions of convergence. Second, the location and orientation of the convergence lines are calculated by analogy with the moment of inertia. Specially, using all unmasked grid points within a defined box (8.25° latitude/longitude, equivalent to ± 5 grid points; Fig. 3a), the moment of inertia and the centroid of mass are calculated where, by analogy, the convergence replaces the mass (Fig. 3b). This analogous tensor I is called the convergence inertia tensor and is defined here by

$$
\begin{bmatrix} I_{xx} & I_{yy} \\ I_{xy} & I_{yy} \end{bmatrix}, \quad \text{where}
$$
$$
I_{xx} = \sum_i c_i x_i^2, \quad I_{yy} = \sum_i c_i y_i^2, \quad I_{xy} = \sum_i c_i x_i y_i.
$$

Here I_{xx}, I_{yy}, and I_{xy} are sums of the convergence at each grid point c_i weighted by products of the distances in the x and y directions to the centroid. The eigenvalues and eigenvectors of the convergence inertia tensor are calculated (Fig. 3c). The larger eigenvalue and its corresponding eigenvector define the orientation of the major axis of convergence within the box (i.e., the along-line direction; Fig. 2b), while the eigenvector associated with the smaller eigenvalue defines the perpendicular axis (i.e., across line direction, Fig. 2c). Last, a bilinear interpolated polynomial is fitted to the convergence field in the across line (i.e., minor eigenvector) direction to determine and locate the convergence maximum, if one exists (Figs. 3d,e).

The technique adopted here improves that used in Berry and Reeder (2014). They took the first derivatives of the divergence (in the x and y directions) and summed them, and then used the second derivative to determine which stationary points were local minima. Their method resulted in a slight bias to northwest–southeast-oriented lines. While their method worked well in the
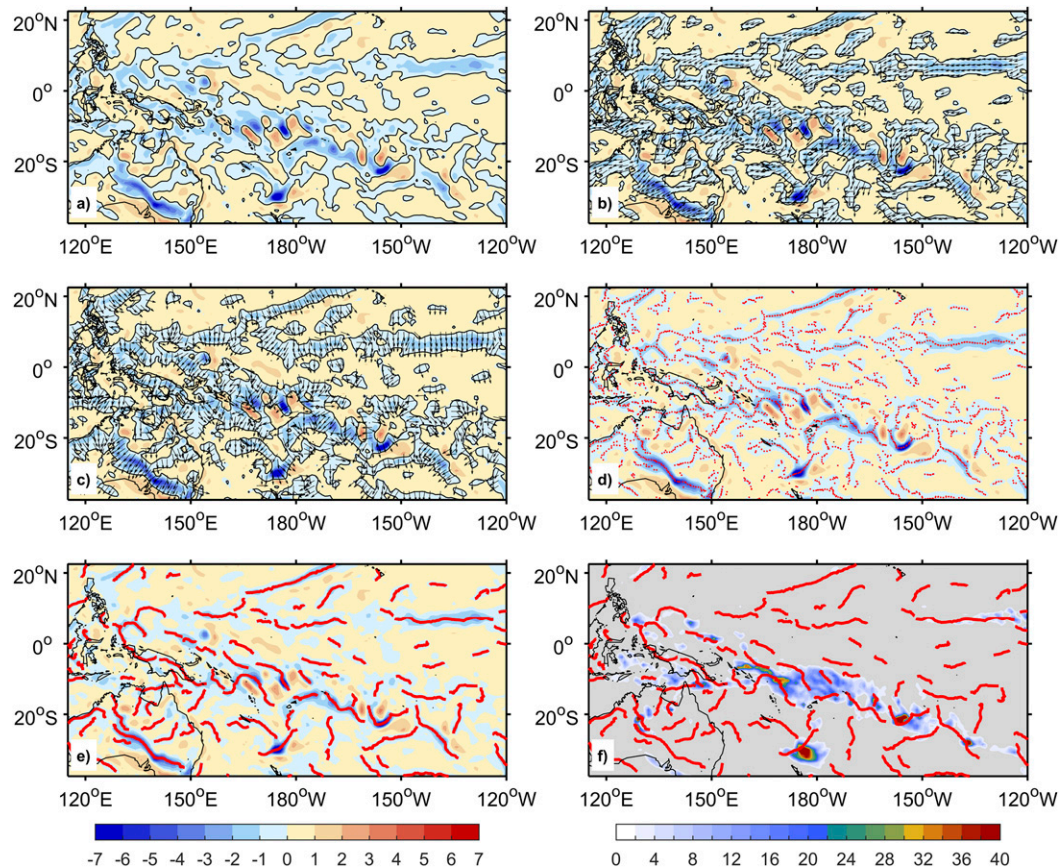
FIG. 2. Example of the procedure employed to objectively identify convergence lines using an instantaneous divergence field over the Pacific Ocean and Australian landmass. (a) Convergent regions are isolated and (b),(c) the components of the inertia tensor relative to the center of convergence using all convergence points in a box are calculated to obtain the eigenvalues and eigenvectors of the inertia tensor. (d) The locations of convergence maxima are located, and (e) a line-joining algorithm joins the maxima into coherent lines. (f) Objectively identified convergence lines are overlaid on satellite imagery to show the association with precipitation.

tropics, this bias increases with latitude. Using the eigenvectors of the inertia tensor eliminates this bias.

Once all convergence maxima are identified in a 6-hourly field (i.e., Fig. 2d), the line-joining algorithm used by Berry et al. (2011a) is employed. This algorithm joins the maxima into coherent lines assuming neighboring points are sufficiently close (here we use a threshold of less than 1° to join points to their nearest neighbor) and the resulting lines meet a minimum length threshold (here we use a threshold of 300 km along the respective line of joined points) (Fig. 2e). The objectively identified lines are shown to coincide with regions of precipitation when overlaid on satellite imagery for the same time (Fig. 2f). The frequency of occurrence of the instantaneous convergence lines over the globe from 60°S to 60°N is calculated. To assess the robustness of the objective detection method, the sensitivity of the identified convergence lines to the imposed threshold

parameters (such as the maximum convergence, the box size used to calculate the centroid, and the minimum length of an identified line) is also examined.

To associate rainfall with the objectively identified convergence lines we first determine the location of grid points with rainfall greater than zero for each 6-hourly field. For each rain grid point, a 2° × 2° box centered on the point is searched for an identified convergence line. If there is at least one convergence line in the box, then the rainfall at that grid point is assumed to be associated with a convergence line. The 6-hourly times are then aggregated to determine how much of the daily rainfall is associated with convergence lines at each grid point. This daily rainfall is expressed as a percentage of the total rainfall. The main difference between the method used here and that by Catto et al. (2012) used to associate rainfall with fronts, is the size of the search box. We employ a smaller search box size primarily due to the higher temporal and spatial
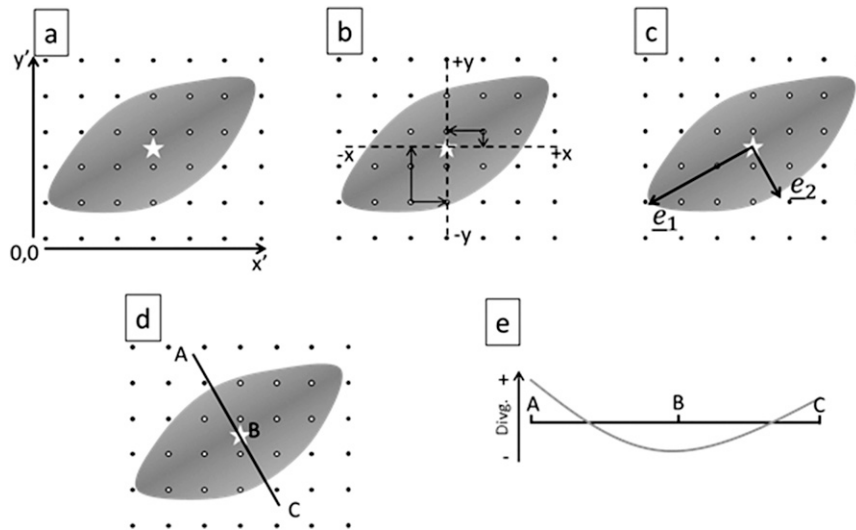
FIG. 3. Schematic showing the method employed to detect locations of divergence minima in the instantaneous field by (a)–(c) calculating the components of inertia tensor relative to a convergence centroid, using all convergence points in the box, to obtain the eigenvalues and eigenvectors of inertia tensor. The larger eigenvalue and corresponding eigenvector describes the orientation of the major axis of convergence within the box (i.e., the along line direction), while the smaller pair describes the perpendicular (i.e., across-line direction). (d),(e) A bilinear interpolated polynomial is fit to the convergence field along the across line (i.e., minor eigenvector) direction to determine and locate a divergence minimum, if one exists.

resolution of the data utilized in the current study. This smaller search box allows a higher degree of confidence in associating rainfall with convergence lines owing to the closer relationship between local-scale convergence and rainfall (Birch et al. 2014a). In addition, fronts are usually tilted, and their rainfall can often extend well ahead of or behind the actual front (Catto et al. 2012). Overall, the 2° search box size allows only the same grid point or adjacent grid points of rainfall to be allocated to a convergence line when it is in close proximity; similar to Catto et al. (2012), the size is a compromise between missing convergence lines for small search areas or counting convergence lines that are too far removed from the rain grid point with too large a search area. Sensitivity tests found that while the choice of search box did not change the spatial pattern of associated rainfall, it did alter the magnitude and is presented in the results. For example, over the region equatorward of 60° the proportion of rainfall allocated to convergence lines using 1°, 2°, and 3° search boxes are 55%, 71%, and 96%, respectively.

3. Results

a. Frequency of convergence lines

The annual-mean frequency and seasonal variability of instantaneous convergence lines greater than 300 km in

length identified in the ERA-Interim dataset over the period 1979–2013 are shown in Fig. 4. The overall pattern and seasonality over the tropics are consistent with previous studies (Waliser and Gautier 1993; Berry and Reeder 2014). Nonetheless, compared to Berry and Reeder (2014), the increased temporal resolution and fewer and weaker constraints (e.g., a shorter line length threshold) result in more lines being detected. The annual-mean frequency (Fig. 4a), expressed as the percentage of time a convergence line is present in each 0.75° × 0.75° grid box, shows that the largest values are of the order of 20% and occur within the ITCZs in all three ocean basins. Because of the higher resolution of the ERA-Interim dataset in comparison to earlier studies, a double ITCZ is also more evident in all basins with a frequency around 10%–15% (Zhang 2001; Liu and Xie 2002; Meenu et al. 2007; Zhang et al. 2007). The lowest values, less than 5%, are found on the eastern flank of the subtropical highs, whereas in the midlatitudes a thin band of lower frequency occurs at approximately 40° in both hemispheres, generally on the southern flank of where dry air descends in the atmospheric overturning circulation. Over land, small regions with high frequency coincide with the major monsoonal systems of India, northern Australia, Africa, and South America.

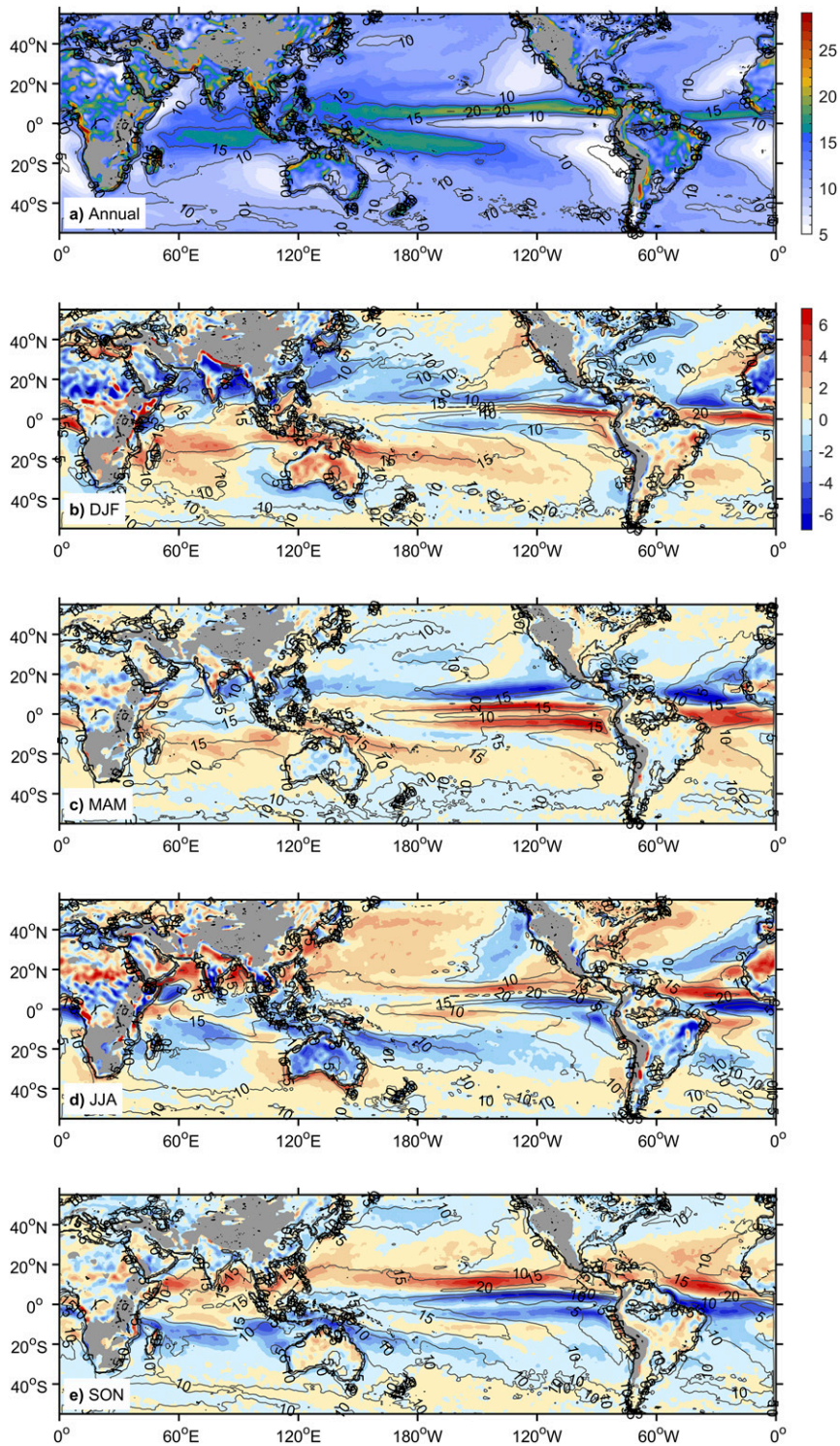The mean seasonal evolution of convergence lines is shown by the 3-month mean anomalies from the annual

FIG. 4. (a) Annual-mean and (b)–(e) seasonal-mean frequency of objectively identified convergence lines (>300 km in length; percentage per month with line in each 0.75° × 0.75° box). Seasonal frequency is shown as the difference from annual (shading) and absolute mean frequency (contours). Regions where the surface topography is higher than 1 km have been shaded gray.
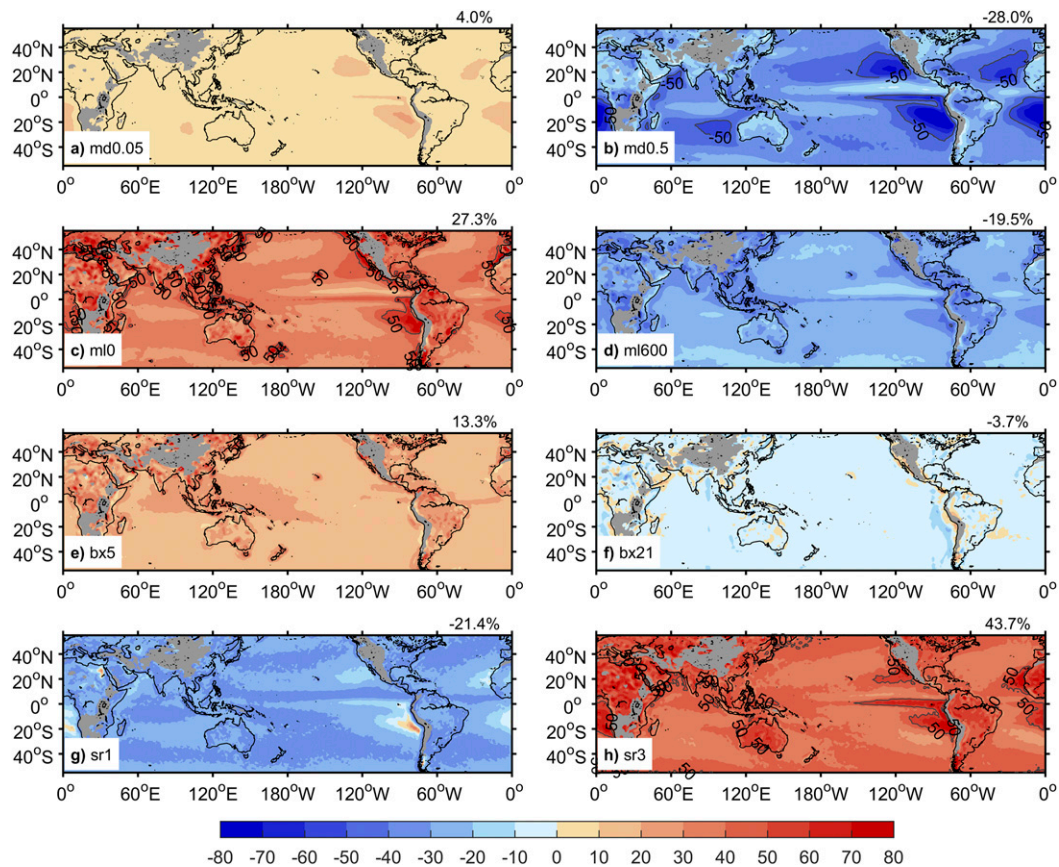
FIG. 5. Sensitivity of annual-mean convergence line frequency to changes in threshold parameters of (a),(b) minimum divergence for masking the instantaneous divergence field, (c),(d) minimum length of convergence line, and (e),(f) search box size for determining the convergence centroid. All differences are shown as the percentage change from Fig. 4a with the mean change given at the top right of each map. (g),(h) Sensitivity of annual-mean proportion of precipitation associated with convergence lines to changes in the size of the search box shown as the percentage change from Fig. 6a with the mean change given at the top right of each map.

mean from December–February (DJF) to September–November (SON) in Figs. 4b–e. Overall, these maps highlight a seasonal cycle in which the oceanic convergence lines migrate meridionally and land-based convergence lines form predominantly during summer. Convergence lines in the ITCZ south of the equator in the eastern Pacific are most frequent in boreal spring [March–May (MAM)], occurring around 20% of the time. They are less frequent in all other seasons, the least frequent being around 5% in boreal fall (SON). Indeed, the weak double ITCZ patterns on the annual-mean frequency across all basins appear to be related to a signature of their seasonal migrations and intensifications.

The sensitivity of the identified convergence lines to the imposed threshold parameters in the automatic detection method is shown in Figs. 5a–f. The changes are expressed as the percentage change from Fig. 4a where the maximum convergence, the box size used to

calculate the convergence centroid, and the minimum length of an identified line are $-0.1 \times 10^{-5}\,\mathrm{s}^{-1}$, 11×11 grid points, and $300\,\mathrm{km}$, respectively. The global mean change for the individual sensitivity test is given at the top right of each map. Relaxing the minimum divergence to include weaker convergence (i.e., $-0.05 \times 10^{-5}\,\mathrm{s}^{-1}$) for masking the instantaneous divergence field does not significantly increase the number of identified convergence lines (Fig. 5a). Conversely, increasing the minimum divergence threshold (i.e., $-0.5 \times 10^{-5}\,\mathrm{s}^{-1}$), which masks weaker convergence regions, leads to large decreases (50%–60%) over regions where the frequency is low (approximately 5%) such as the eastern flank of the subtropical highs (Fig. 5b). Similarly, Fig. 5c highlights that where convergence lines occur infrequently, especially over the eastern Pacific and Atlantic Oceans, they are relatively short, as evidenced by the increase in frequency when the length threshold is omitted. The frequency also increases over land when examining

convergence lines of any length, suggesting that topography causes lines to become more fragmented than over the ocean. Doubling the minimum length threshold of convergence lines to 600 km results in a decrease of nearly 20% globally, more so over land and the adjacent coastal waters such as the Maritime Continent. This decrease further highlights that shorter lines generally occur over these regions (Fig. 5d). Last, adjusting (decreasing and increasing) the box size used to calculate the convergence centroid of the unmasked divergence field has only a small influence on the frequency of identified convergence lines (Figs. 5e,f). A nearly spatially uniform change is found in both cases of decreasing and increasing the size, except for slightly larger increases of occurrence over land and the Indo-Pacific warm pool when the box is reduced to 5×5 grid points (equivalent to 3.75° latitude/longitude).

b. Association of precipitation with convergence lines

Combining precipitation data with the convergence line locations allows the precipitation to be attributed to these rainfall-related features. The annual-mean and seasonal-mean global distributions of the proportion of precipitation associated with convergence lines for the period 1998–2013 are shown in Fig. 6. The annual map should be interpreted as identifying regions where there is a strong dynamical coupling between convergence lines and precipitation (Fig. 6a). For example, in most regions of high rainfall, such as in the ITCZ, more than 75% of rainfall is attributed to convergence lines greater than 300 km in length. Similar maximum proportions of precipitation are also evident in the regions of the midlatitudes, even though here the convergence line frequency is lower than in the tropics. Over the rest of the oceans, the proportion is still relatively high, generally greater than about 65%. Over land, values range between 30% and 60%, and the lowest proportions of precipitation (less than 15%) associated with convergence lines occur on the eastern flank of the subtropical highs. The sensitivity of the proportion of precipitation associated with convergence lines to the imposed search box size is shown in Figs. 5g and 5h as the percentage change from Fig. 6a. Decreasing the search box size (from 2° to 1° latitude/longitude; Fig. 5g) used to associated convergence lines with precipitation has less influence than an increase (from 2° to 3° latitude/longitude; Fig. 5h). However, when using a larger search box size, the largest increases occur in regions where the proportion of precipitation associated with convergence lines is relatively low, resulting in a large percentage change. This result highlights that 2° latitude/longitude is a suitable threshold for the datasets used as the proportions do not change drastically when the search box

size is reduced, but any larger and the precipitation seems to be unrealistically associated with convergence lines far removed.

The mean seasonal variations from the annual-mean precipitation associated with convergence lines shows variations of up to 30% throughout the year (Figs. 6b–e). These large variations highlight the regions where the association increases (red) or decreases (blue) during the seasons and where it mainly varies in proportion to the frequency of convergence lines. The largest seasonal variations occur over the tropical eastern Pacific and Atlantic Oceans; here generally more than 75% of precipitation is associated with convergence lines in MAM, but this reduces to about 40% in SON. The proportion of precipitation associated with convergence lines in the SPCZ varies only slightly throughout the year, with values being 5%–10% larger in JJA and SON and 5%–10% smaller in the other two seasons. Increases on the eastern flanks of the subtropical highs occur during wintertime and are accompanied by decreases over the adjacent land area, such as over northern Africa and North America in DJF (Fig. 6b), and over Australia and South America in JJA (Fig. 6d).

The results above only consider the proportion of precipitation associated with well-defined convergence lines (greater than 300 km in length). Figure 7 shows the annual-mean global distributions of the residual proportion of precipitation associated with shorter, more fragmented lines (less than 300 km in length; Fig. 7b), and the proportion of precipitation that is not associated with any convergence line (Fig. 7c). For comparison, the proportion of precipitation associated with convergence lines greater than 300 km in length is repeated in Fig. 7a, and the mean values over the region equatorward of 60° are given at the top right of each map. On average, only about 13% of precipitation is associated with shorter convergence lines, with larger values over land (20%–35%) than over the ocean (5%–15%). This difference may be due to the diurnal cycle having a greater influence over land and adjacent ocean water than in open ocean regions, reducing the time for local-scale convergence to organize into larger features and an increase in noise (Hendon and Woodberry 1993; Yang and Slingo 2001). The residual proportion of precipitation not associated with any convergence lines averaged over the map is under 30% (Fig. 7c) and occurs primarily in regions with both low precipitation (indicated by contours enclosing regions less than 1 mm day^{-1}) and low frequency of convergence lines. In these regions, the proportion of precipitation not associated with any convergence lines is up to 60%, whereas lower values between 15%–20% occur elsewhere, the lowest being in the ITCZs. It is noted that, although the proportion of
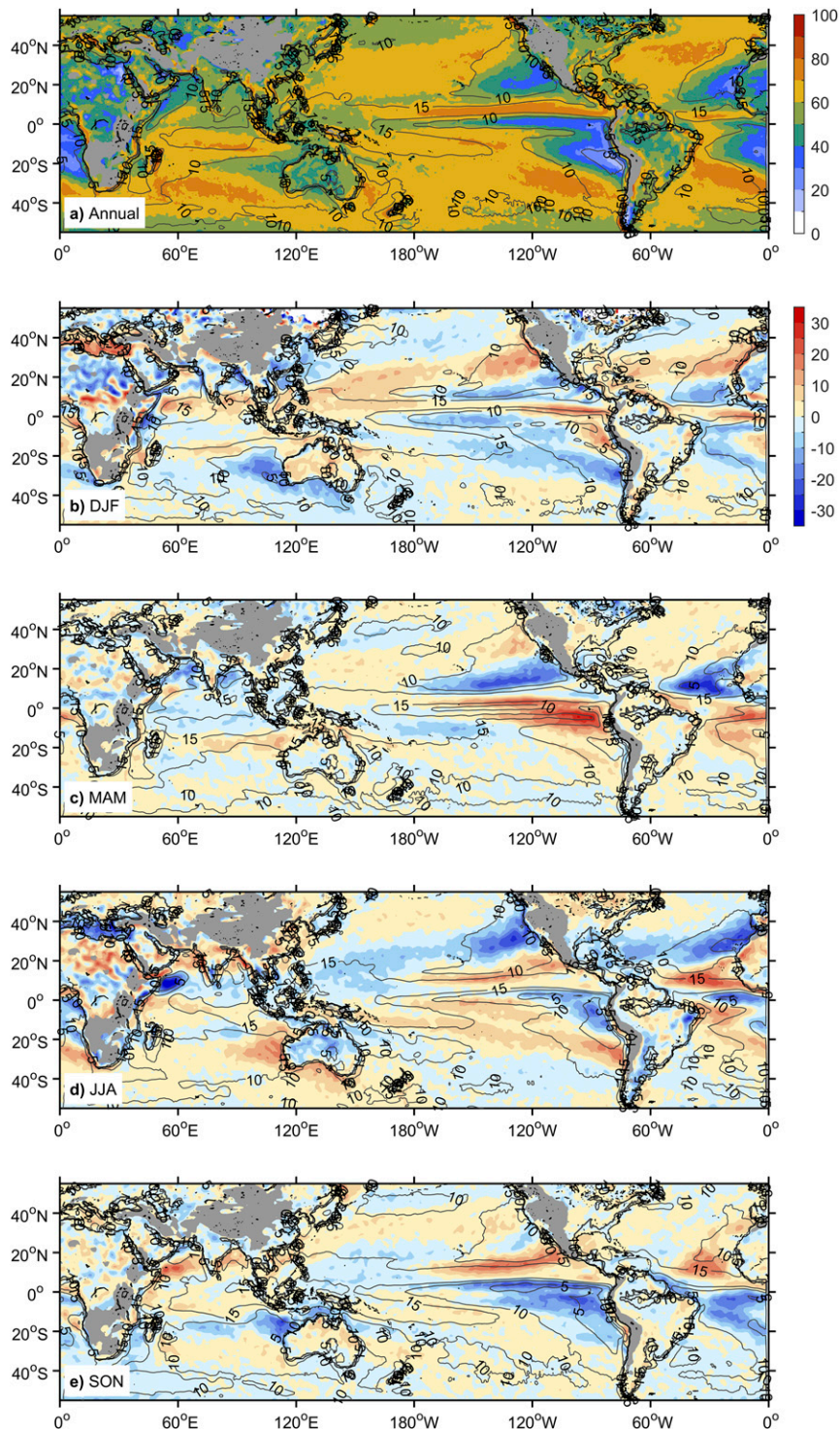
FIG. 6. (a) Annual-mean and (b)–(e) seasonal-mean proportion of precipitation (percentage) associated with convergence lines (shading) and the frequency of lines (contours, as in Fig. 4, but for 1998–2013). Seasonal proportion of precipitation is shown as a difference from annual. Regions where the surface topography is higher than 1 km have been shaded gray.
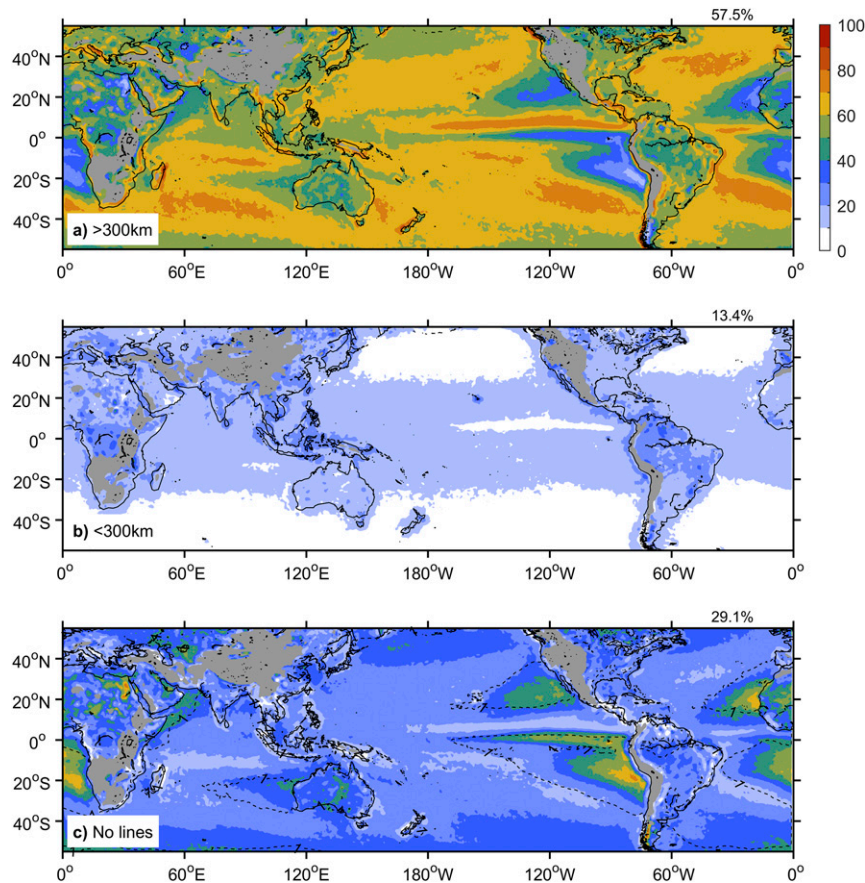
FIG. 7. Annual-mean proportion of precipitation (percentage) associated with convergence lines (a) greater than and (b) less than 300 km. (c) The residual proportion of precipitation not associated with any convergence lines (shaded) and areas where the daily rainfall is less than 1 mm day^{-1} (dashed contours). The global mean proportion is given at the top-right of each map and regions where the surface topography is higher than 1 km have been shaded gray.

precipitation associated with long coherent and shorter convergence lines changes with changing search box size, the same conclusions can be drawn. For example, the mean proportion of precipitation associated with long coherent convergence lines (i.e., 57% using a search box size of 2° latitude/longitude) ranges from 43% to 83% for search box sizes of 1° and 3° latitude/longitude, respectively. The proportion of precipitation associated with the shorter convergence lines and that not associated with any convergence lines have ranges of 12%–13% and 4%–45%, respectively. Overall, only a small increase results from using 2° over 1°; however, using a search box size of 3° results in a much larger increase in attributable precipitation to long coherent convergence lines, further supporting our choice.

To highlight some of the key relationships found in the study, the precipitation and convergence associated with identified convergence lines has been calculated for several locations. Figures 8a and 8b show the high correlation between the strength of convergence and the precipitation amounts over the western and eastern equatorial Pacific Oceans, respectively. In addition, the length of the identified convergence lines (indicated by the color of the data points) also has a strong relationship with both fields. In particular, stronger convergence and heavier precipitation is generally associated with more well-defined, long convergence lines over these tropical ocean regions. The sensitivity of this relationship (indicated by the slope ratio) is twice as strong in the western equatorial Pacific Ocean than in the east, primarily due to the greater precipitation there, which is a consequence of the higher SSTs and increased moisture availability. On the other hand, although similar relationships exist for regions over land, such as equatorial Africa (Fig. 8c) and the Maritime Continent (Fig. 8d), the range of values is smaller than over the ocean regions, and the convergence lines are generally much shorter or fragmented. Birch et al. (2014b) found
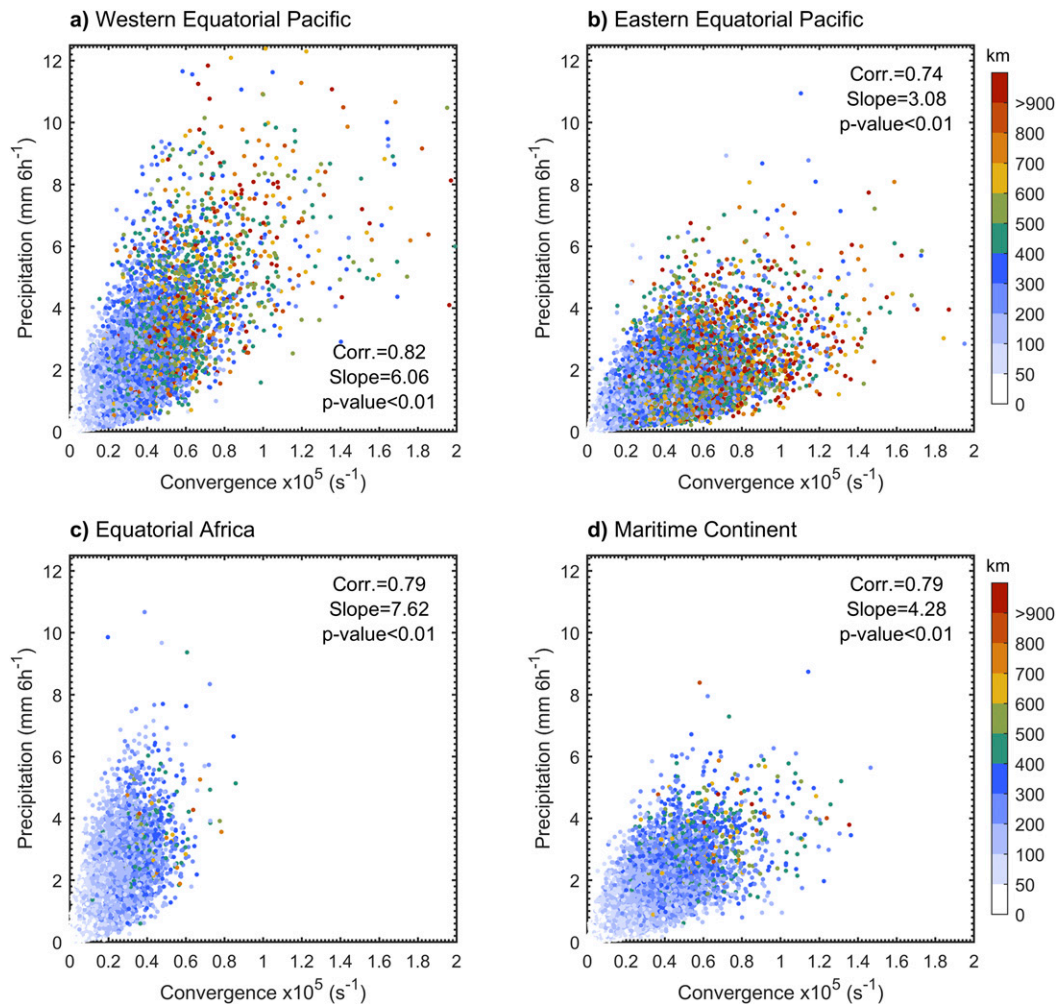
FIG. 8. Mean convergence (s^{-1} scaled by 10^5) of the objectively identified convergence lines and the associated precipitation over the (a) western and (b) eastern equatorial Pacific, (c) equatorial Africa, and (d) Maritime Continent. The color of each data point depicts the length of the convergence line (km).

that although lines derived from the ERA-Interim reanalysis are consistent with those derived from satellite imagery, they were somewhat under resolved and weaker. Therefore the sensitivity of the relationship in Fig. 8 may change with different datasets, especially for small-scale features.

4. Discussion and conclusions

In the present study a new automated, objective method is derived to identify low-level convergence lines in gridded datasets of the horizontal wind field. By combining it with satellite-derived global gridded precipitation data we quantify the proportion of global precipitation associated with such coherent lines. The overall spatial pattern and seasonality of convergence lines over the tropics remain similar to those in previous

studies (Berry and Reeder 2014), highlighting the reproducibility of the objective method given some modifications. Specifically, by utilizing reanalysis output with increased temporal resolution, and imposing fewer (e.g., omitting lower troposphere temperature thresholds to isolate tropical features) and weaker (e.g., a shorter length threshold) constraints, the present study also allows for an examination of the instantaneous relationship between precipitation and convergence in the lower troposphere, which varies substantially on regional and even subdaily scales (Bain et al. 2010).

Over the tropical oceans, a large percentage of precipitation is associated with convergence lines, with stronger convergence and heavier precipitation generally associated with more well-defined, longer convergence lines. Over land and the adjacent ocean waters, less precipitation is associated with convergence lines.
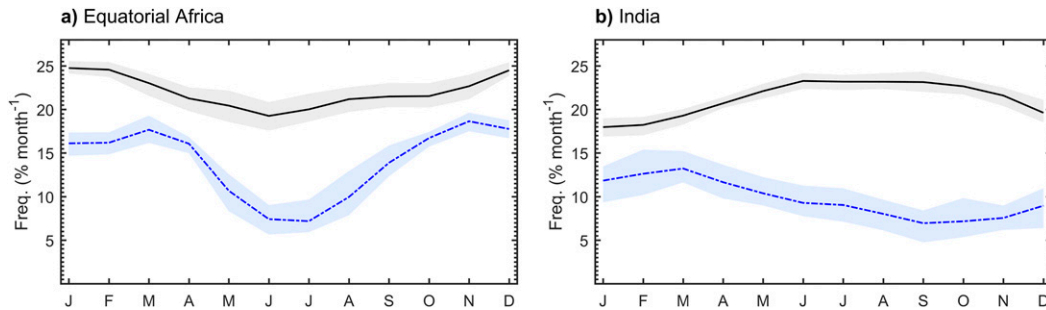
FIG. 9. Mean seasonal cycle of the frequency (lines) and 10%–90% range across years (shading) of all (black) objectively identified convergence lines, and only those associated with precipitation (blue) over (a) northern equatorial Africa (0°–10°N, 10°–35°E) and (b) India (5°–25°N, 70°–85°E).

This change in the proportion appears to be a result of more shorter or fragmented convergence lines over land and the adjacent waters, where an increase in noise from the diurnal cycle and topography may act to reduce the time and space for local-scale convergence to organize into larger well-organized features. The change in the proportion may also be due to systematic biases in the precipitation dataset used. For example, although CMORPH captures the spatial precipitation distribution patterns well, some biases include overestimation in the tropic to subtropics, underestimation in the middle to high latitudes, and overestimation (underestimation) of weak (strong) intensities (e.g., Joyce and Xie 2011). These influences need to be taken into consideration when interpreting the results of the present study. Nonetheless, the proportion of precipitation not associated with any convergence line primarily occurs where both the amount of precipitation and frequency of convergence lines are low.

The present study is useful for understanding the regional relationships between organized low-level convergence and rainfall over both ocean and land. Nonetheless, some results appear counterintuitive, especially over some land regions. For example, precipitation over equatorial Africa is generally governed by the seasonal movement of the ITCZ (Nicholson 2000; Preethi et al. 2015). For this reason, the rainfall in the equatorial region is greatest during the two transition seasons (i.e., MAM and SON), and greatest in each tropical margin during the summer of the respective hemispheres (i.e., JJA in the north and DJF in the south). However, the seasonal cycle of all convergence lines has a minimum over north equatorial Africa during JJA and a maximum in DJF (black line in Fig. 9a). Similarly, the frequency of convergence lines associated with precipitation is also lower in JJA (blue line in Fig. 9a). This result is physically sensible as longer coherent convergence lines may be more organized in the

ITCZ, and are generally associated with increased precipitation intensity (Fig. 8). During DJF, there are more convergence lines (Fig. 9a), although they are presumably smaller. Hence, an increase in the number of shorter convergence lines may be associated with decreased precipitation at this time of year. This conclusion appears to also apply for India, which has the opposite seasonal cycle. Over India the number of convergence lines is greatest during JJA (black line in Fig. 9b), despite some negative anomalies in the southern central region (Fig. 4d). This spatial pattern in the convergence line frequency anomalies agrees well with the areas of greatest precipitation during this time of year (e.g., the southwest coast and northeastern interior of India; Goswami et al. 2006). However, although the frequency of all convergence lines increases in JJA over India, once again there are fewer lines associated with precipitation (blue line in Fig. 9b). This result further supports the idea that more organized (and longer) convergence lines are associated with greater rainfall.

One advantage of using instantaneous fields to construct the climatology of the relationship between rainfall and organized convergence is that it allows the diurnal cycle to be investigated, among other things. Mesoscale convergence lines produced by the diurnal cycle of continental heating and cooling are thought to play an important role in the initiation and organization of clouds and convection in the tropics (Hendon and Woodberry 1993; Yang and Slingo 2001). Figure 10 shows an example of the diurnal variation of convergence lines and precipitation over the Maritime Continent and Australian region. At 0000 UTC (approximately midmorning) the convergence lines lie almost wholly offshore of the islands such as Sumatra, Java, Borneo, and New Guinea, coinciding with the heaviest precipitation (Figs. 10a,b). These offshore convergence lines are presumably connected land breezes and gravity waves. By 1200 UTC
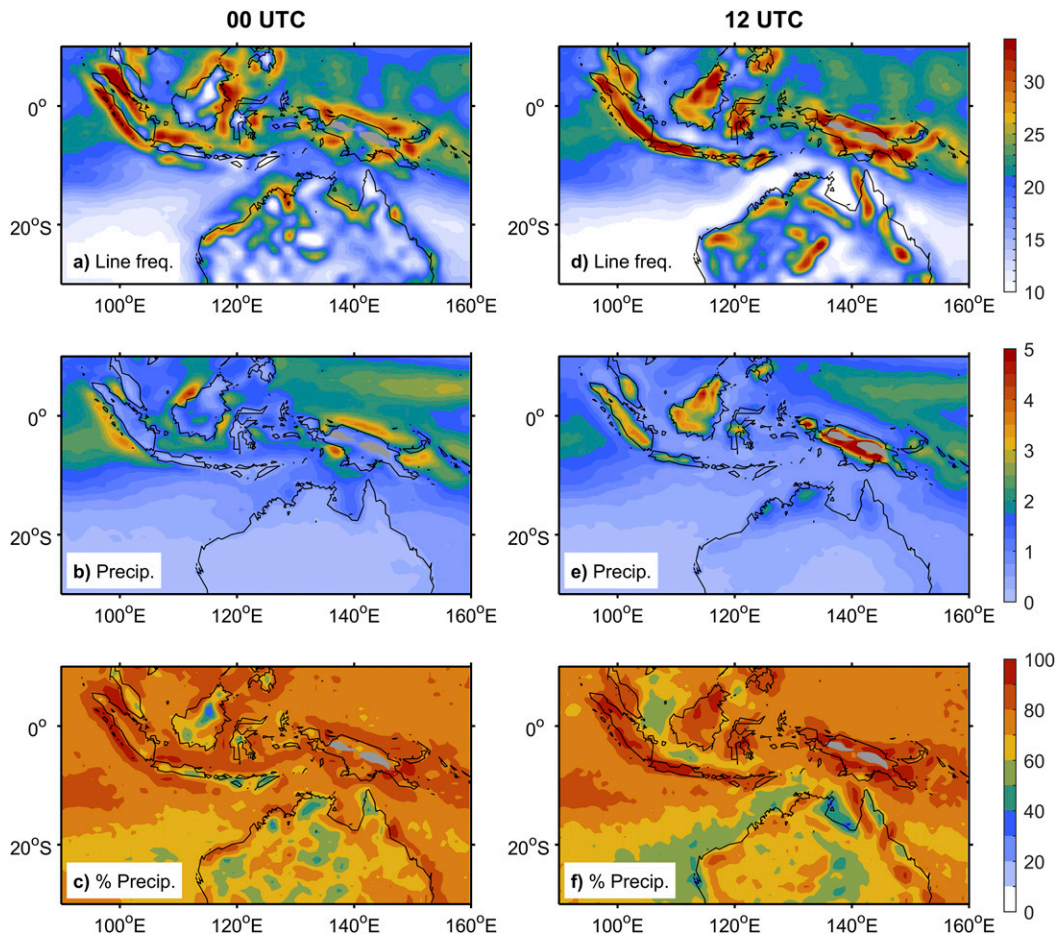
FIG. 10. Diurnal cycle shown at (left) 0000 and (right) 1200 UTC of the (a),(d) annual-mean frequency of objectively identified convergence lines (% month with line in each $0.75° \times 0.75°$ box), (b),(e) annual-mean CMORPH precipitation [mm (6 h)$^{-1}$], and (c),(f) annual-mean proportion of precipitation (percentage) associated with convergence lines. Regions where the surface topography is higher than 1 km have been shaded gray.

(approximately late evening) most convergence lines and the heaviest precipitation lie over the islands and northern Australia (Figs. 10d,e). These onshore convergence lines are presumably associated with the thermally driven upslope circulation and sea breezes. Over the open ocean regions there is little change in the frequency over the day. The proportion of precipitation associated with convergence lines captures this diurnal variation (Figs. 10c,f), highlighting that the location of the local-scale convergence is a significant determinant of the local-scale precipitation.

Under greenhouse warming, regional dynamical precipitation changes are projected to be in spatial contrast to much of that associated with thermodynamic increases in moisture (Bony et al. 2013; Chadwick et al. 2013; Widlansky et al. 2013; Wills et al. 2016). Therefore it is of great interest to better understand the underlying dynamical processes responsible for initiation of

convection and the subsequent development of precipitation. It also an important issue for the evaluation of global climate models and their projections of precipitation changes. There is some consistency between the models on the increase in global mean precipitation per degree of global warming due to counteracting changes in net tropospheric radiative cooling and latent heating (Stephens 2005; Lambert and Webb 2008), although the level of agreement is weaker at the regional scale (Rowell 2012; Chadwick et al. 2013). This weakened level of agreement may be a consequence of how well the models simulate the dynamical precipitation change, among other model errors, owing to their poor simulation of convection. For example, although average global composites of precipitation produced by models can be in agreement with observations, this agreement can result from opposing errors, such as producing precipitation that is too light too often

([Stephens et al. 2010](#)). However, such models may be able to represent well the aspects of the circulation, such as low-level convergence, important for large proportions of the precipitation, providing an insightful measure of the model performance and better understanding of how regional precipitation may change. The method of the present study can be used to attempt to answer such issues by applying it to global climate models, which is currently underway. The initial results show that the frequency and proportion of the precipitation associated with convergence lines in climate models is less than reported here. This result is presumably due to lower resolution in the climate models, even though the general patterns and many large-regional features are well represented. This is the case when the analysis is repeated with the ERA-Interim precipitation in place of CMORH. In this case, the proportion of precipitation associated with convergence lines is reduced by about 10%, as there are fewer small-scale and high-intensity precipitation features.

REFERENCES

Bain, C. L., G. Magnusdottir, P. Smyth, and H. Stern, 2010: Diurnal cycle of the intertropical convergence zone in the east Pacific. *J. Geophys. Res.*, **115**, D23116, doi:[10.1029/2010JD014835](#).

——, J. De Paz, J. Kramer, G. Magnusdottir, P. Smyth, H. Stern, and C.-C. Wang, 2011: Detecting the ITCZ in instantaneous satellite data using spatiotemporal statistical modelling: ITCZ climatology in the east Pacific. *J. Climate*, **24**, 216–230, doi:[10.1175/2010JCLI3716.1](#).

Berry, G., and M. J. Reeder, 2014: Objective identification of the intertropical convergence zone: Climatology and trends from the ERA-Interim. *J. Climate*, **27**, 1894–1909, doi:[10.1175/JCLI-D-13-00339.1](#).

——, C. Jakob, and M. J. Reeder, 2011a: Recent global trends in atmospheric fronts. *Geophys. Res. Lett.*, **38**, L21812, doi:[10.1029/2011GL049481](#).

——, M. J. Reeder, and C. Jakob, 2011b: A global climatology of atmospheric fronts. *Geophys. Res. Lett.*, **38**, L04809, doi:[10.1029/2010GL046451](#).

Birch, C. E., J. H. Marsham, D. J. Parker, and C. M. Taylor, 2014a: The scale dependence and structure of convergence fields preceding the initiation of deep convection. *Geophys. Res. Lett.*, **41**, 4769–4776, doi:[10.1002/2014GL060493](#).

——, M. J. Reeder, and G. J. Berry, 2014b: Wave-cloud lines over the Arabian Sea. *J. Geophys. Res. Atmos.*, **119**, 4447–4457, doi:[10.1002/2013JD021347](#).

——, M. Roberts, L. Garcia-Carreras, D. Ackerley, M. J. Reeder, A. Lock, and R. Schiemann, 2015: Sea breeze dynamics and convection initiation: The influence of convective parameterization in weather and climate model biases. *J. Climate*, **28**, 8093–8108, doi:[10.1175/JCLI-D-14-00850.1](#).

Bony, S., G. Bellon, D. Klocke, S. Sherwood, S. Fermepin, and S. Denvil, 2013: Robust direct effect of carbon dioxide on tropical circulation and regional precipitation. *Nat. Geosci.*, **6**, 447–451, doi:[10.1038/ngeo1799](#).

——, and Coauthors, 2015: Clouds, circulation and climate sensitivity. *Nat. Geosci.*, **8**, 261–268, doi:[10.1038/ngeo2398](#).

Catto, J. L., C. Jakob, G. Berry, and N. Nicholls, 2012: Relating global precipitation to atmospheric fronts. *Geophys. Res. Lett.*, **39**, L10805, doi:[10.1029/2012GL051736](#).

——, ——, and N. Nicholls, 2013: A global evaluation of fronts and precipitation in the ACCESS model. *Aust. Meteor. Oceanogr. J.*, **63**, 191–203.

——, ——, and ——, 2015: Can the CMIP5 models represent winter frontal precipitation? *Geophys. Res. Lett.*, **42**, 8596–8604, doi:[10.1002/2015GL066015](#).

Chadwick, R., I. Boutle, and G. Martin, 2013: Spatial patterns of precipitation change in CMIP5: Why the rich do not get richer in the tropics. *J. Climate*, **26**, 3803–3822, doi:[10.1175/JCLI-D-12-00543.1](#).

Collins, M., and Coauthors, 2013: Long-term climate change: Projections, commitments and irreversibility. *Climate Change 2013: The Physical Science Basis*, T. F. Stocker et al., Eds., Cambridge University Press, 1029–1136.

Dee, D. P., and Coauthors, 2011: The ERA-Interim reanalysis: Configuration and performance of the data assimilation system. *Quart. J. Roy. Meteor. Soc.*, **137**, 553–597, doi:[10.1002/qj.828](#).

Flato, G., and Coauthors, 2013: Evaluation of climate models. *Climate Change 2013: The Physical Science Basis*, T. F. Stocker et al., Eds., Cambridge University Press, 741–866.

Goswami, B. N., V. Venugopal, D. Sengupta, M. S. Madhusoodanan, and P. K. Xavier, 2006: Increasing trend of extreme rain events over India in a warming environment. *Science*, **314**, 1442–1445, doi:[10.1126/science.1132027](#).

Hastenrath, S., 1995: *Climate Dynamics of the Tropics*. Kluwer Academic, 488 pp.

Hendon, H. H., and K. Woodberry, 1993: The diurnal cycle of tropical convection. *J. Geophys. Res.*, **98**, 16 623–16 637, doi:[10.1029/93JD00525](#).

IPCC, 2007: *Climate Change 2007: The Physical Science Basis*. Cambridge University Press, 996 pp.

Jakob, C., 2010: Accelerating progress in global atmospheric model development through improved parameterizations: Challenges, opportunities, and strategies. *Bull. Amer. Meteor. Soc.*, **91**, 869–875, doi:[10.1175/2009BAMS2898.1](#).

——, 2014: Going back to basics. *Nat. Climate Change*, **4**, 1042–1045, doi:[10.1038/nclimate2445](#).

Joyce, R. J., and P. Xie, 2011: Kalman filter-based CMORPH. *J. Hydrometeor.*, **12**, 1547–1563, doi:[10.1175/JHM-D-11-022.1](#).

——, J. E. Janowiak, P. A. Arkin, and P. Xie, 2004: CMORPH: A method that produces global precipitation estimates from passive microwave and infrared data at high spatial and temporal resolution. *J. Hydrometeor.*, **5**, 487–503, doi:[10.1175/1525-7541(2004)005<0487:CAMTPG>2.0.CO;2](#).

Lambert, F. H., and M. J. Webb, 2008: Dependency of global mean precipitation on surface temperature. *Geophys. Res. Lett.*, **35**, L16706, doi:[10.1029/2008GL034838](#).

Lindzen, R. S., and S. Nigam, 1987: On the role of sea surface temperature gradients in forcing low-level winds and convergence in the tropics. *J. Atmos. Sci.*, **44**, 2418–2436, doi:[10.1175/1520-0469(1987)044<2418:OTROSS>2.0.CO;2](#).

Liu, W. T., and X. Xie, 2002: Double intertropical convergence zones—A new look using scatterometer. *Geophys. Res. Lett.*, **29**, 2072, doi:10.1029/2002GL015431.

Meenu, S., K. Rajeev, K. Parameswaran, and C. Suresh Raju, 2007: Characteristics of the double intertropical convergence zone over the tropical Indian Ocean. *J. Geophys. Res.*, **112**, D11106, doi:10.1029/2006JD007950.

Nicholson, S. E., 2000: The nature of rainfall variability over Africa on time scales of decades to millennia. *Global Planet. Change*, **26**, 137–158, doi:10.1016/S0921-8181(00)00040-0.

Preethi, B., T. P. Sabin, J. A. Adedoyin, and K. Ashok, 2015: Impacts of the ENSO Modoki and other tropical Indo-Pacific climate-drivers on African rainfall. *Sci. Rep.*, **5**, 16653, doi:10.1038/srep16653.

Reeder, M. J., and R. K. Smith, 1998: Mesoscale meteorology. *Meteorology of the Southern Hemisphere*, D. Vincent and D. J. Karoly, Eds., Amer. Meteor. Soc., 201–241.

——, ——, D. J. Low, J. Taylor, S. J. Arnup, L. C. Muir, and G. Thomsen, 2013: Diurnally forced convergence lines in the Australian tropics. *Quart. J. Roy. Meteor. Soc.*, **139**, 1283–1297, doi:10.1002/qj.2021.

Rowell, D., 2012: Sources of uncertainty in future changes in local precipitation. *Climate Dyn.*, **39**, 1929–1950, doi:10.1007/s00382-011-1210-2.

Rybka, H., and H. Tost, 2014: Uncertainties in future climate predictions due to convection parameterisations. *Atmos. Chem. Phys.*, **14**, 5561–5576, doi:10.5194/acp-14-5561-2014.

Stephens, G. L., 2005: Cloud feedbacks in the climate system: A critical review. *J. Climate*, **18**, 237–273, doi:10.1175/JCLI-3243.1.

——, and Coauthors, 2010: Dreary state of precipitation in global models. *J. Geophys. Res.*, **115**, D24211, doi:10.1029/2010JD014532.

Stevens, B., and S. Bony, 2013: What are climate models missing? *Science*, **340**, 1053–1054, doi:10.1126/science.1237554.

Waliser, D. E., and C. Gautier, 1993: A satellite-derived climatology of the ITCZ. *J. Climate*, **6**, 2162–2174, doi:10.1175/1520-0442(1993)006<2162:ASDCOT>2.0.CO;2.

Widlansky, M. J., P. J. Webster, and C. D. Hoyos, 2011: On the location and orientation of the South Pacific convergence zone. *Climate Dyn.*, **36**, 561–578, doi:10.1007/s00382-010-0871-6.

——, A. Timmermann, K. Stein, S. McGregor, N. Schneider, M. H. England, M. Lengaigne, and W. Cai, 2013: Changes in South Pacific rainfall bands in a warming climate. *Nat. Climate Change*, **3**, 417–423, doi:10.1038/nclimate1726.

Wills, R. C., M. P. Byrne, and T. Schneider, 2016: Thermodynamic and dynamic controls on changes in the zonally anomalous hydrological cycle. *Geophys. Res. Lett.*, **43**, 4640–4649, doi:10.1002/2016GL068418.

Wodzicki, K. R., and A. D. Rapp, 2016: Long-term characterization of the Pacific ITCZ using TRMM, GPCP, and ERA-Interim. *J. Geophys. Res. Atmos.*, **121**, 3153–3170, doi:10.1002/2015JD024458.

Yang, G. Y., and J. Slingo, 2001: The diurnal cycle in the tropics. *Mon. Wea. Rev.*, **129**, 784–801, doi:10.1175/1520-0493(2001)129<0784:TDCITT>2.0.CO;2.

Zhang, C., 2001: Double ITCZs. *J. Geophys. Res.*, **106**, 11 785–11 792, doi:10.1029/2001JD900046.

Zhang, X., W. Lin, and M. Zhang, 2007: Toward understanding the double intertropical convergence zone pathology in coupled ocean–atmosphere general circulation models. *J. Geophys. Res.*, **112**, D12102, doi:10.1029/2006JD007878.